Terahertz Detection with Perfectly-Absorbing Photoconductive Metasurface

Thomas Siday,[1] Polina P. Vabishchevich,[2,3] Lucy Hale,[1] Charles Thomas Harris,[2,3]

Ting Shan Luk,[2,3] John L. Reno,[2,3] Igal Brener,[2,3] Oleg Mitrofanov,[1,2,]*

[1] University College London, Electronic and Electrical Engineering, London, WC1E 7JE UK

[2] Center for Integrated Nanotechnologies, Sandia National Laboratories, Albuquerque, NM 87123, USA

[3] Sandia National Laboratories, Albuquerque, NM 87185, USA

KEYWORDS: terahertz, perfect absorption, metasurface, photoconductive detector

ABSTRACT:

Terahertz (THz) photoconductive devices are used for generation, detection and modulation of THz waves, and they rely on the ability to switch electrical conductivity on a sub-picosecond time scale using optical pulses. However, fast and efficient conductivity switching with high contrast has been a challenge, because the majority of photoexcited charge carriers in the switch do not contribute to the photocurrent due to fast recombination. Here, we improve efficiency of electrical conductivity switching using a network of electrically connected nano-scale GaAs resonators, which form a perfectly-absorbing photoconductive metasurface. We achieve perfect absorption without incorporating metallic elements, by breaking the symmetry of cubic Mie resonators. As a result, the metasurface can be switched between conductive and resistive states with extremely high contrast using an unprecedentedly low level of optical excitation. We integrate this metasurface with a THz antenna to produce an efficient photoconductive THz detector. The perfectly-absorbing photoconductive metasurface opens paths for developing a wide range of efficient optoelectronic devices, where required optical and electronic properties are achieved through nanostructuring the resonator network.

With wireless communications and imaging systems progressing steadily towards the terahertz (THz) frequency range, recent research in the field is increasingly focused on the development of more efficient THz devices for generation, detection, and modulation of THz waves.[1-6] A key technology for existing photonic devices operating in the terahertz (THz) frequency range is an ultrafast photoconductive (PC) switch, an optoelectronic element, which changes electrical conductivity under illumination between a highly resistive (OFF) and highly conductive (ON) state within a sub-picosecond time period.[7,8] The PC switch performance relies on three essential requirements: (1) a sub-picosecond recombination time for photo-excited charge carriers, (2) a high contrast in conductivity for the ON and OFF states, and (3) an efficient conversion of photons to charge carriers. To produce an efficient PC switch, all three requirements must be met simultaneously.

To date, research on material growth and post-growth material treatment have solved the first challenge through incorporation of charge trapping centers in the material.[8] For example, low-temperature (LT) growth and post-grow annealing have reduced the recombination time in GaAs by orders of magnitude, to below 1 ps. Whilst this was achieved with high conductivity contrast,[8] the conversion efficiency in the original ultrafast switches has been low. The low conversion efficiency comes from the PC material properties: to absorb the maximum number of photons, the PC material must be optically thick, however, most of the photo-excited charge carriers recombine before they can drift across the PC layer.

In recent years, several groups have attempted to improve the conversion efficiency through the PC switch architecture,[9] by integrating plasmonic nanostructures. They successfully enhanced photo-excitation of charge carriers through optical field concentration close to the electrodes[9-17] and through photon trapping.[18,19] However, the device architecture with plasmonic

nanostructures often leads to reduced conductivity contrast between the OFF and ON states. Furthermore, plasmonic nanostructures introduce significant Ohmic losses, limiting the conversion efficiency[20] and leading to low device damage threshold. These effects negate the effectiveness gained by integrating plasmonic nanostructures in the PC switch architecture.

We wondered whether another PC switch architecture may provide a solution to effective photo-excitation without problematic plasmonic structures, since many functionalities enabled by plasmonic nanostructures can be realized by means of recently introduced all-dielectric metasurfaces.[21–28] All-dielectric metasurfaces typically consist of planar arrays of nano-scale dielectric Mie resonators, which can fully absorb incident light for selected wavelengths.[29–36] To assess the potential of all-dielectric metasurfaces for improving efficiency of ultrafast PC switches, here we develop an all-dielectric metasurface, which efficiently absorbs light and, at the same time, forms an electrically connected network, where conductivity changes under optical excitation between OFF and ON states quickly and with high contrast. To achieve efficient photo-excitation (i.e. to meet Requirement 3) without incorporating metallic elements, we develop a perfectly-absorbing metasurface by breaking the symmetry of cubic Mie resonators. We meet Requirement 2 through the design of the resonator network, obtaining a contrast in conductivity of over 10^7 between the ON and OFF states. To ensure fast switching (Requirement 1), we fabricated this PC metasurface from LT-GaAs, where the recombination time for photo-generated charge carriers (due to interband electron excitation at 800 nm) is shorter than one picosecond.[8] With all three requirements met, we integrate the metasurface with a THz antenna and demonstrate detection of THz pulses with more than six orders of magnitude signal-to-noise ratio (SNR) using an unprecedentedly low level of ultrafast laser excitation (100 μW). We also verify that the switching time remains short enough to enable detection up to a frequency of 3 THz. We thus show that the

PC switch architecture incorporating an all-dielectric metasurface provides a solution for improving efficiency of THz PC detectors.

The key improvement in our design is that of *perfect absorption* within an optically thin metasurface. Typically, perfect absorption in an optically thin metasurface is achieved by introducing a metallic back reflector.[29–32] Such an architecture however is not compatible with THz detectors because the metallic layer would block THz waves. We therefore consider an alternative approach proposed only recently: an all-dielectric metasurface can be perfectly-absorbing if it supports two resonant modes of opposite symmetry, odd and even with respect to the metasurface plane, provided that the two modes are degenerate and critically-coupled.[36,37] For comparison, a metasurface which supports modes displaying only one symmetry, absorbs a maximum of 50% of incoming photons.[37] To achieve perfect absorption in our PC metasurface, we therefore need to design an optical resonator supporting modes of odd and even symmetry simultaneously. A nanoscale cube supports a set of resonant Mie modes, where the lowest frequency mode is the magnetic dipole (MD) mode.[38] Due to the cubic symmetry, there are three degenerate MD modes, and we will describe these modes by the direction of the magnetic dipole vector M.[38] Two of the modes have their dipole moments, M_x and M_y, in the xy-plane, with the corresponding electric field distributions being odd with respect to the metasurface plane; the dipole moment of the third mode M_z is orthogonal to the plane, with the corresponding field distribution being even with respect to the plane (Figure 1a). Although the cubic resonator supports MD modes of both symmetries, unfortunately, the MD mode M_z does not couple to a plane wave with the k-vector normal to the xy-plane, i.e. this mode is dark. Only the modes with odd symmetry, M_x and M_y, can be directly excited by this plane wave, and therefore perfect absorption using only MD modes in cubic dielectric resonators is impossible. Here, we find a way to simultaneously excite the MD

modes with both odd and even symmetries, in particular M_x and M_z, and thus realize perfect absorption, through breaking the resonator cubic symmetry. Detailed analysis of the modes within the structure is provided in *Supporting Information*.

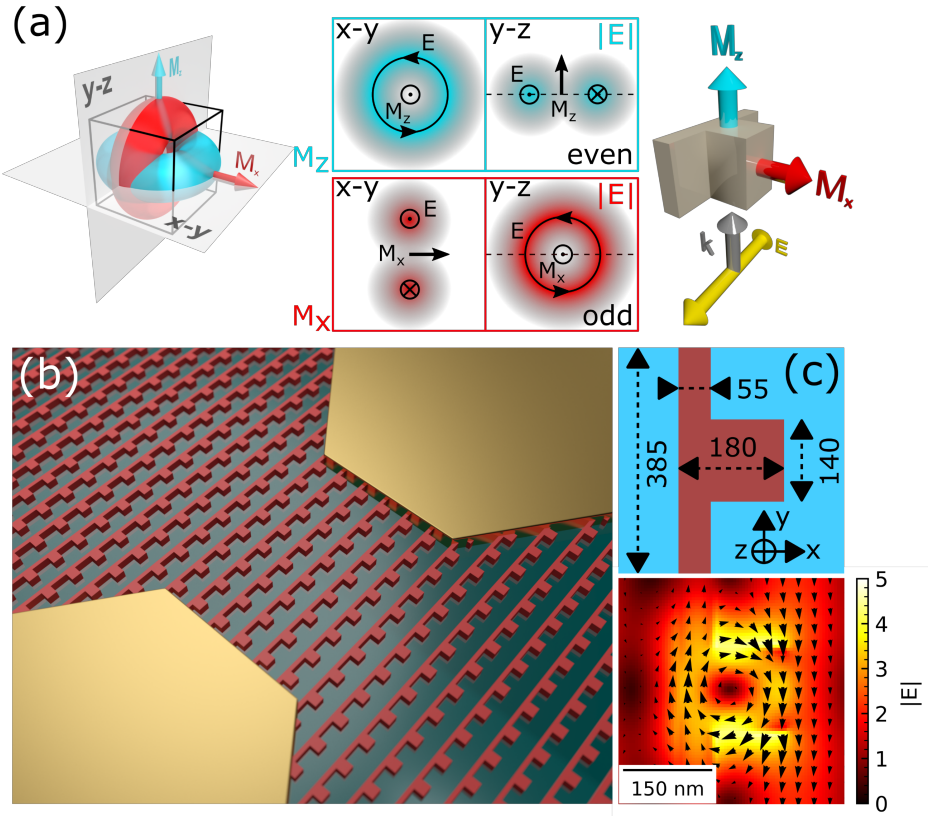

Figure 1. (a) Magnetic dipole (MD) Mie modes, M_x and M_z, in a cubic resonator (*left panel*); the corresponding electric field distributions in *xy*- and *yz*-planes are shown schematically in the *middle panel*. The electric field distribution is even with respect to the *xy*-plane for M_x: $E(z) = E(-z)$, and odd for M_z: $E(z) = -E(-z)$. The MD mode M_x can be excited by a *y*-polarized plane wave propagating in *z*-direction, whereas the MD mode M_z is dark for the light at normal incidence. In contrast, the two modes can be excited by a *y*-polarized wave propagating in *z*-direction, in a cubic resonator with broken symmetry, e.g. with a bar attached to one side (*right panel*). (b) Conceptual illustration of the perfectly-absorbing photoconductive metasurface comprising a network of resonators with broken symmetry and integrated into a THz detector. (c) Resonator schematic with dimensions in nm (*top panel*); and simulated electric field distribution in the *xy*-plane, at the mid-height of the resonator (*bottom panel*), showing the distinctive circulating electric field of the MD mode M_z under excitation with a *y*-polarized plane wave at normal incidence. The dimensions are for a GaAs resonator (n=3.6) surrounded by a uniform low-index medium (n=1.57), where perfect absorption is achieved at 800 nm.

To enable excitation of the dark MD mode M_z by a *y*-polarized plane wave, we introduce a continuous bar along one side of the resonator, as shown in Figure 1a. The bar breaks the cubic symmetry and leads to excitation of the otherwise dark mode.[24–26] The incident plane wave also excites the M_x mode, and thus both odd and even MD modes are excited simultaneously in such a resonator. At the same time, the bar allows photo-excited charge carriers to flow along the *y*-axis to neighboring resonators, making the metasurface electrically conductive (Figure 1b).

To confirm that it is possible to excite the two MD modes by a *y*-polarized plane wave, we simulate an infinite array of the resonators shown in Figure 1c using a commercial-grade software based on the finite-difference time-domain method.[39] First, we simulate a symmetric metasurface consisting of an array of GaAs resonators placed in a uniform dielectric medium, so that the metasurface has a mirror plane symmetry (*xy*-plane). We use the refractive index of optical epoxy (n = 1.57) to emulate the metasurface substrate. We will show later that a practical implementation of this metasurface, where air (n = 1) replaces the epoxy for the half-space x>0, and thus breaks the mirror symmetry, performs similarly, due to the relatively high refractive index of the GaAs resonator (n = 3.68) compared to the optical epoxy substrate (n = 1.57) and air (n = 1) environment. We find optimal dimensions of the resonator by monitoring absorption in the structure, as perfect absorption requires that the resonant frequencies for M_x and M_z be aligned, and that the condition of critical coupling be satisfied for the two modes simultaneously.[36,37] Figure 1c summarizes the optimal dimensions that enable perfect absorption at λ=800 nm for GaAs metasurface only 200 nm thick.

In Figure 2a we illustrate numerically that indeed, both modes M_x and M_z are excited by the plane wave impinging on the metasurface at normal incidence. The magnitude $|H|$, and

components H_x and H_z clearly show the two modes with similar magnitudes. For comparison, we also show the field distributions for a cubic resonator (i.e. without the side bar), where the MD mode M_z is not present, whilst excitation of M_x still occurs (Figure 2b). In both cases, the H_y component is negligible, and it is therefore not shown.

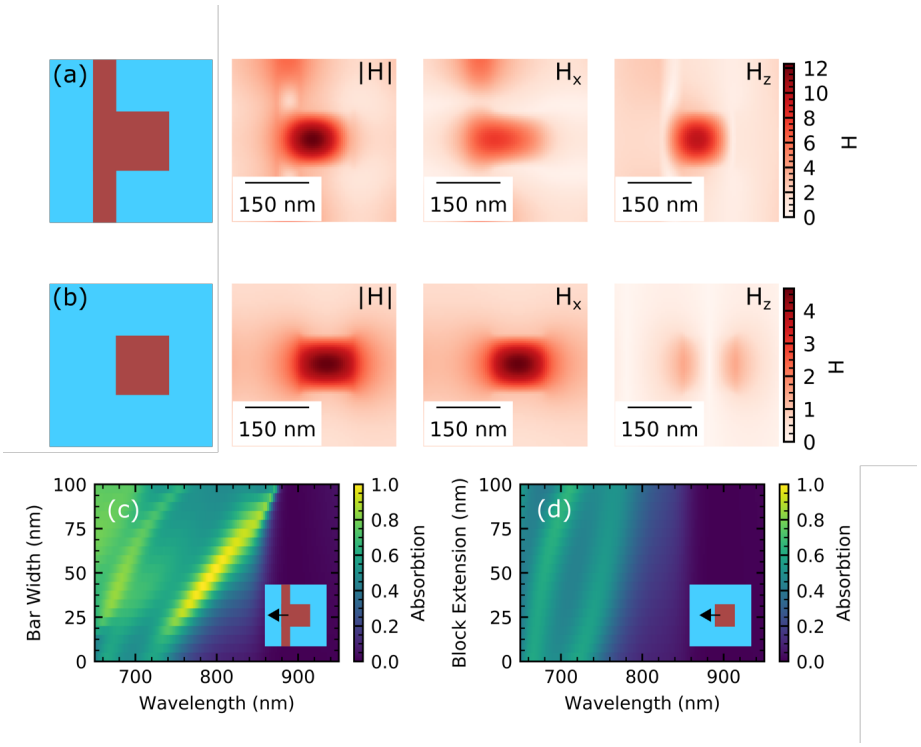

Figure 2. (a) Numerically simulated magnetic field distribution in the resonator with broken symmetry showing two components H_x and H_z of similar magnitude, corresponding to the MD modes M_x and M_z. The field maps are shown in the *xy*-plane at the midpoint of the resonator. (b) Magnetic field distribution for a rectangular (symmetric) resonator showing only the MD mode M_x for the same excitation conditions. (c, d) Absorption in resonators with asymmetric (c) and symmetric shapes (d) as a function of wavelength and width of the bar/rectangular extension: the asymmetric design (c) exhibits a strong absorption band, which shifts from 750 nm to 850 nm as the width of the bar is increased; perfect absorption is achieved near 800 nm.

The concurrent excitation of the MD mode M_z with the MD mode M_x in the resonator with broken symmetry has a striking effect on the absorption spectrum. Nearly perfect absorption occurs within a relatively narrow absorption band for bar widths between 40 and 70 nm (Figure

2c). This perfect absorption is possible only for *y*-polarized light, whereas the orthogonal polarization (*x*) is not absorbed by the metasurface as efficiently. The polarization dependence is consistent with the fact that the *x*-polarized plane wave excites only one MD mode, M_y, and not M_z. Weak absorption in the case of excitation of a single mode is evident in the absorption spectrum map for an array of symmetric rectangular blocks (Figure 2d), where we varied the width of the block (along the *x*-axis) to facilitate comparison with Figure 2c. Only one mode, the MD mode M_x, is excited in the symmetric rectangular block; as a result, only a weak absorption band near the bandgap edge of GaAs (around 730-760 nm) is visible in the map. Absorption in this case is much lower, as predicted for a resonator supporting only one mode.[37,38] Our simulation results confirm that we enable perfect absorption for *y*-polarized light at normal incidence by breaking the symmetry of cubic resonators, which leads to simultaneous excitation of the MD modes M_z and M_x.

We now evaluate absorption in a practical implementation of our metasurface design, where metasurface has air (n=1) on one side and a substrate on the other side (n=1.57); and confirm numerically that the metasurface in air exhibits a similar behavior. In Figure 3a, we show calculated reflectivity, transmission and absorption spectra for the structure with the dimensions in Fig. 1(c). As in Figure 2, the absorption spectrum exhibits a similar peak: absorption reaches 98% at 799 nm.

It is useful to put these results in perspective and compare the maximum absorption of the metasurface to that of unstructured GaAs layers: a uniform 200 nm thick GaAs film absorbs less than 30% of incident photons at 800 nm (Figure 3a, *green line*), whereas an infinitely thick layer of GaAs absorbs ~70%, the latter being limited due to Fresnel reflection from the air-GaAs

interface. Therefore, our metasurface enables higher absorption than can be achieved with unstructured GaAs of any thickness.

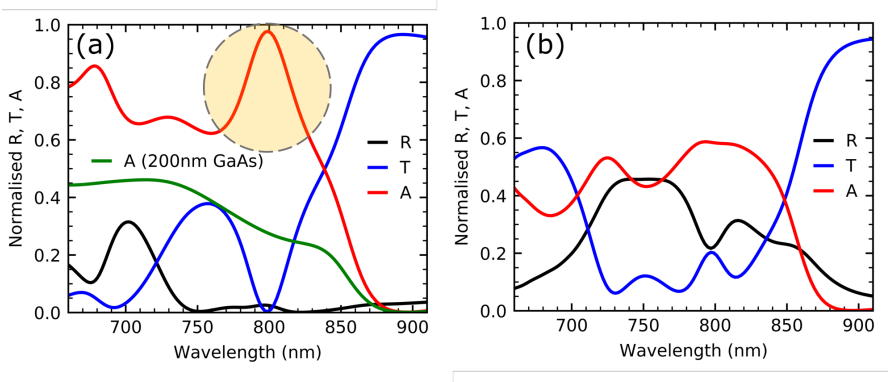

Figure 3. Simulated absorption (*red*), reflectivity (*black*) and transmission (*blue*) spectra for the metasurface made of 200 nm thick GaAs. (a) For *y*-polarized light at normal incidence, an absorption peak at 800 nm (*highlighted*) rises above absorption in an unstructured 200 nm thick layer of GaAs (*green*). The peak corresponds to the MD mode M_z. (b) For *x*-polarized light, the incident wave excites the MD mode M_y, whereas M_z remains unexcited, and absorption at 800 nm is significantly lower.

Using the simulation results, we select optimal resonator dimensions (Figure 1c) to achieve maximum absorption at 800 nm, the typical wavelength of ultrafast Ti:Sapphire lasers, and experimentally test performance of such a metasurface. We characterize wavelength-dependent transmission and absorption properties of several metasurface samples (see *Methods*), one of which is illustrated in Fig. 4(a), and find their transmission properties to be similar to the simulations. In Figure 4b,c, we show representative normalized transmission spectra of the metasurface in Figure 4a for *y*-polarized and *x*-polarized light respectively (*solid blue lines*). The transmission spectra show reasonable agreement with the numerical results in Figure 3; in particular, transmission decreases below 5% near 820nm, indicating efficient resonant absorption for the *y*-polarized light, whereas the decrease is not as strong for the orthogonal polarization. The spectra also show some differences: the minimum transmission occurs at 820 nm, rather than at

800 nm, and the linewidth of the resonance for *y*-polarized excitation is broader than in the numerical simulations. We attribute the difference between the simulations and experimental observations to three factors: inhomogeneous broadening due to resonator size variations in the array, a larger average size of the fabricated resonators compared to the design, and the presence of in-plane *k*-vector components in the focused beam. The first factor is evident in electron micrographs, which show that resonator dimensions vary within the array (see Figure 4a and Figure S1). The second factor, i.e. a larger average size of resonators, is difficult to confirm experimentally due to the limited resolution in the micrograph images, nevertheless we note that the resonance wavelength scales with resonator size, and therefore we expect a wavelength shift of 20 nm for a relatively small increase of 2-3% in the resonator size. Lastly, the third factor requires a more detailed look at the effect of focusing the probe beam for experimental characterization of transmission. Unlike the plane wave used in simulations, the optical beam is focused to a spot less than 10 μm in diameter (see *Methods*), and it has *k*-vector components in the xy-plane, which can excite the dark mode M_z directly. To quantify the effect of focused beam excitation, we simulate transmission properties of the entire metasurface using a focused Gaussian beam illumination. The simulations confirm the differences we observed experimentally: the absorption spectrum broadens, and the maximum absorption is reduced to 80%. For comparison, we also display transmission (*solid blue line*) in the same sample for the orthogonal polarization in Figure 4c. As we expect, the orthogonal polarization experiences weaker absorption as it passes though the metasurface. While it is difficult to evaluate absorption directly in the experiment, we measure photoconductivity for a wavelength range between 750 and 820 nm (*red dots*) and we find that, indeed, excitation with a *y*-polarized focused laser beam raises the photoconductivity of the metasurface by approximately one half in comparison with a *x*-polarized excitation.

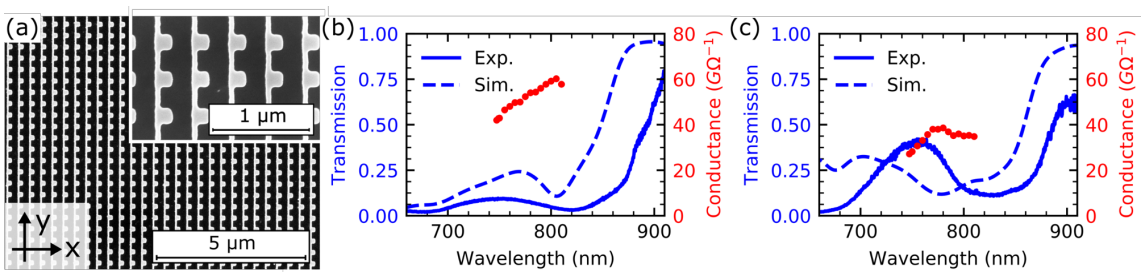

Figure 4. Experimental characteristics of the metasurface. (a) Scanning electron micrograph of a metasurface with individual resonators shown magnified in the inset. (b,c) Transmission and photoconductivity spectra for *y*-polarized and *x*-polarized light respectively. The spectra represent transmission averaged over the beam spot area, which is similar in size to the area shown in (a). For comparison, dashed lines show numerically simulated transmission spectra for the focused beam illumination, which can excite M_z directly. Red dots show photoconductivity spectra of the metasurface measured using ultrafast laser excitation (~150 fs, 200 μW average power) focused between electrical contacts separated by 3 μm).

With the optical properties of fabricated metasurfaces confirmed, we proceed to integrate the metasurface between the electrodes of a THz PC antenna, as shown in the SEM micrograph in Figure 5a (see Figure S2 for large scale images of the antenna), and test the performance of the metasurface THz detector using a THz time-domain spectroscopy (TDS) system (see *Methods*). We detect time-domain waveforms of THz pulses generated in a ZnTe crystal (Figure 5b) and find that the metasurface detector produces a noticeably higher photocurrent output compared to conventional THz detectors for an average excitation power of only P_g = 100 μW (*y*-polarized) (see *Supporting Information* for detailed comparison) . Even at this low level of excitation, we begin observing the onset of absorption saturation. Figure 5c illustrates the saturation effect in a plot of THz-field induced peak photocurrent as a function of average power of the optical excitation beam (*red*). Figure 5c also shows the root-mean squared (RMS) noise of the photocurrent measured at a frequency of 2.7 kHz, which is a typical modulation frequency used

for lock-in photocurrent detection (see *Methods*). The noise increases linearly at higher optical excitation powers (>100 μW), and thus we attribute the main noise source to fluctuations of the laser power. We find that the maximum signal to noise ratio (SNR) is achieved at P_g = 100 μW, which is approximately one order of magnitude lower than what is observed for similar THz PC detectors without the metasurface.[15,20] Furthermore, in direct comparison with the results in Mitrofanov *et al*.[28], we find that SNR obtained with the metasurface detector is ~ 10 times higher for P_g = 100 μW (see *Supporting Information*). It is worth noting here that the metasurface detectors exhibit very high dark resistance (~50 GΩ) in comparison to detectors based on unstructured LT GaAs layers (~1 GΩ). The higher resistance leads to a higher ON/OFF switching contrast (>10^7) and better SNR at low optical excitation powers. We thus conclude that the low optical excitation power required for the optimum SNR performance is due to the efficient optical absorption as well as the high dark resistance of the metasurface.

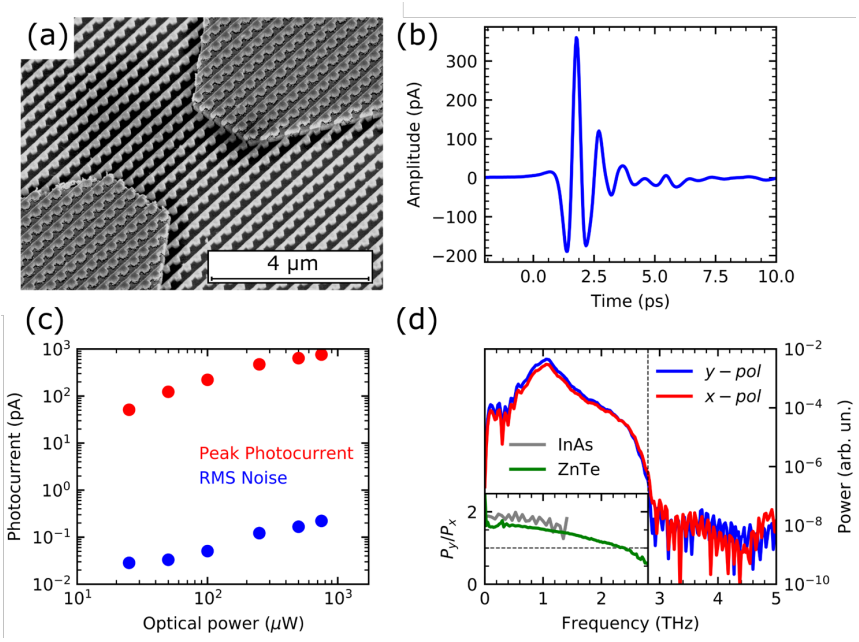

Figure 5. Characteristics of the photoconductive THz detector with integrated perfectly-absorbing metasurface. (a) SEM of the photoconductive area of the detector showing tips of the THz antenna, which serve also as electrical contacts. (b) THz pulse waveform measured with the THz detector using *y*-polarized

optical gating pulses of average power of 100 μW. (c) Peak THz photocurrent (red) and root-mean squared (RMS) noise (blue) as functions of average power of the optical gate beam. (d) Power spectral density (PSD) obtained by Fourier transform of detected THz pulse waveforms for two orthogonal polarizations of the optical gating pulses. The inset shows the PSD ratio for the two polarizations (*y*-polarized/*x*-polarized) for frequencies up to 2.9 THz, above which SNR<10. The PSD ratio is independent of the incident THz pulse waveform as confirmed by using different THz pulses generated using InAs and ZnTe crystals.

Finally, we evaluate potential drawbacks of the metasurface-based THz detector, which could originate from the resonant nature of the perfect absorption effect. Since the optical fields oscillate within the resonators before being absorbed,[40–42] the THz detection bandwidth could be limited. In particular, coupling to the MD mode M_z could limit the detector frequency response due to a higher *Q*–factor compared to the uncoupled MD mode M_x.[25] However, the Fourier transform of the measured THz pulse waveform in Figure 5d shows that the detector sensitivity range reaches a relatively high frequency of ~3 THz, at which point the measured signal becomes comparable to the noise level. This is a typical frequency response for photoconductive THz detectors, indicating that bandwidth degradation for the metasurface detector is negligible. Nevertheless, we evaluate the effect of the optical field evolution on the bandwidth of the detector experimentally by comparing the THz response for two orthogonal polarizations: for the *y*-polarized excitation the MD mode M_z is excited together with M_x, whereas for the *x*-polarized excitation, only the MD mode M_x is excited. Therefore, the photocurrent rise time for *y*-polarized excitation is longer than that for *x*-polarized excitation. Figure 5(d) compares Fourier transform spectra of the THz pulse detected in the same device using *y*-polarized (*blue line*) and *x*-polarized (*red line*) optical excitation. At low frequencies, the photocurrent power spectral density (PSD) is higher for *y*-polarized excitation, confirming more efficient optical absorption in the metasurface. That enhancement decreases at higher frequencies, and above 2.5 THz, the response of the THz

detector actually becomes stronger for *x*-polarized excitation. This indicates that the higher *Q*-factor of the coupled modes indeed limits the detector performance, albeit only above that frequency. We highlight the bandwidth limiting effect by showing the PSD ratio for the two polarizations in the inset of Figure 5d. We also verify that this effect is independent of the shape of the THz pulse by confirming that different THz pulses, generated using InAs and ZnTe crystals, yield a similar frequency dependence for the PSD ratio (Figure 5d). It is worth noting that the THz detector bandwidth is affected also by the incident optical pulse duration and the photoexcited charge carrier recombination time. In fact, the latter is the most significant bandwidth limiting factor, as the recombination time is several times longer than the evolution of the optical field in the metasurface. Nevertheless, even a relatively small 50 fs increase in the photocurrent rise time due to the high *Q*-factor of the coupled modes still can produce a measurable effect on the bandwidth of the THz detector (see *Supporting Information*), consistent with the observed polarization dependence.

In summary, we developed a perfectly-absorbing photoconductive all-dielectric metasurface, which improves the efficiency and performance of ultrafast photoconductive switches. We integrated this metasurface into photoconductive THz detectors, and achieved THz pulse detection with SNR of more than six orders of magnitude using an unprecedentedly low level of ultrafast laser excitation of 100 μW. We attribute the extremely low switching power and excellent noise performance to perfect-absorption properties of the metasurface as well as its nanostructure, which results in extremely high dark resistivity. We realized perfect absorption without incorporating any metallic structures or back reflectors, by designing a GaAs resonator which supports two degenerate and critically-coupled MD modes. One of the modes has the MD moment normal to the surface and the second mode has the MD moment in the metasurface plane.

Simultaneous excitation of these two modes leads to close-to-perfect optical absorption near the wavelength of λ=800 nm for a 200 nm thick photoconductive resonator network. At the same time, the resonator network enables ultrafast and efficient switching of electrical conductivity with high contrast ratio. The photoconductive metasurface is compatible with practical devices, such as THz emitters, detectors and modulators, and it opens paths for improving their efficiencies and thus impacting practical applications of THz technology, including THz spectroscopy and imaging, and future THz communications.

Methods. *Photoconductive Metasurface Fabrication.* A 200 nm thick layer of GaAs is grown at 250 °C by molecular beam epitaxy (MBE) on top of a semi-insulating GaAs substrate (wafer VA0977) with a GaAs buffer layer and two thin layers of $Al_{0.55}Ga_{0.45}As$ separated by 100 nm. The Al-containing layers serve in the fabrication process as stop-etch layers as described later. The epilayer is then annealed at 600 °C for 40 s in forming gas to achieve high dark resistivity of the material.

Photoconductive (PC) metasurfaces with the pattern shown in Figure 1c are fabricated using electron beam lithography (EBL) and a hard SiO_2 mask. First, the epilayer surface is spin-coated with two layers of photoresist (PMMA495A4/PMMA950A4). The dual photoresist layer facilitates the lift-off process. 20x20 μm^2 patches of the pattern in Figure 1c, repeated with a periodicity of 385 nm, are exposed using a 30 keV electron beam. After optimizing the EBL dosage, we use a dosage of 240 $\mu C/cm^2$ to produce close replicas of the write pattern. The photoresist is developed in a solution of MIBK:IPA (1:3) for 60 s and then rinsed in IPA for 20 s. We then deposit a 30 nm thick layer of SiO_2 using electron beam evaporation in vacuum. The photoresist is removed by soaking the samples in acetone to form the hard SiO_2 mask on the GaAs surface. We then etch the samples with the SiO_2 mask in the BCl_3 inductively coupled plasma

(ICP) reactive ion etching (RIE) system to the depth of ~200 nm. Gas flow rates into the ICP chamber for BCl_3, Ar, and N_2 are 20, 2.5, and 4 cm^3/min, respectively, and the RF power applied to the sample chuck is 240 W. This RIE process produces practically vertical sidewalls for the etched structure (Figure S1). After the etch, the remaining SiO_2 mask is removed using a buffered oxide wet etch (BOE). The etch also removes the passivation layer, which tends to form on the sidewalls during the RIE process.[43]

We note that the EBL dosage affects the shape of the etched features. Specifically, exposures lower than 240 μC/cm^2 made the width of the strip uneven, wider near the cubes and narrower between the cubes; exposures higher than 240 μC/cm^2 introduced some rounding of the structure corners. After SEM inspection of metasurfaces fabricated using a range of exposures, we select samples with dimensions closest to the nominal for fabrication of the THz detectors.

THz Detector Fabrication. Photoconductive THz detectors are built by integrating a THz antenna directly over the metasurface. Two metallic bars in the shape of dipole antenna are lithographically formed using EBL and metal electron beam evaporation. A 3 μm gap between pointed tips of the antenna is positioned at the center of the metasurface patch (Figure 5a). The width of the pointed tips is 3 μm, so that a 3 μm x 3 μm square area of the metasurface between the bars is accessible for photoexcitation. The antenna bars are 200 nm think and 10 μm wide, and the total length of the entire antenna is ~83 μm.

The samples with THz detectors are attached to 0.5 mm thick *z*-cut sapphire substrates using epoxy (EPO-TEC 353ND) with the THz antenna surface facing the sapphire substrate. The epoxy thickness is ~2 μm. After curing the epoxy, the GaAs substrate is thinned by mechanical lapping to the thickness of ~20 μm. The remainder of the substrate is then removed using wet etching in a solution of citric acid and hydrogen peroxide.[44] The etch rate for AlGaAs in the citric

acid etch is significantly slower than that for GaAs. The Al-containing layers introduced during the growth thus allow us to stop the wet etch process when the LT GaAs metasurface is reached. The final sample thus contains a THz antenna with the photoconductive metasurface in the gap, all bonded to the sapphire substrate by the epoxy.

Optical Transmission Measurements. To characterize optical transmission of the metasurface samples, broadband light from an incandescent lamp is passed thought a broadband polarizer and focused on the metasurface using a microscope objective (50X, NA=0.65). The beam size is estimated to be <10 μm in diameter. The transmitted beam is collected by another microscope objective with NA=0.3, passed through another polarizer, and analyzed by a diffraction grating spectrometer. The transmission spectrum is calculated as a ratio of the spectrum measured for light passing through the metasurface and a spectrum measured for light passing through the sapphire substrate. Using the sapphire substrate, rather than no sample, as a reference ensures that the optical path in the confocal system remains unchanged for the sample and the reference measurements. Absorption within the sapphire and the thin layer of epoxy is small in the range of interest (650-950nm), and it is thus neglected.

Dark- and Photo-conductivity Measurements. Dark resistance of the THz PC metasurface detectors is evaluated from *IV* characteristics measured with a semiconductor parameter analyzer. Current between the antenna contacts is measured in a dark chamber with the bias varied from 0 to 50 mV in steps of 0.01 mV. We find the *IV* characteristics linear with the slope corresponding to R~50 GΩ.

Photoconductivity is evaluated for the THz detectors excited by ~160-200 fs pulses generated by a Ti:Sapphire laser with the repetition rate of 80 MHz and the average power of

0.2 mW. The intensity and polarization of the excitation pulses is controlled with a λ/2 waveplate and a broadband polarizer (extinction ratio: 500:1). The laser beam is focused in the antenna gap using an NA=0.5 microscope objective (New Focus 20X). Position of the beam in the gap is optimized to achieve minimum resistance, which was measured by a multimeter. The resistance measurements are repeated as the wavelength of the laser is tuned within the tuning range of the laser (750-820 nm). During this set of measurements, we maintain the FWHM of the laser pulse spectrum at ~6-7 nm, and the average optical power incident on the THz detector at 0.2 mW.

THz Pulse Waveform Measurements. THz detectors are tested using two custom-built THz time-domain spectroscopy (TDS) systems driven by Ti:Sapphire lasers. In one system, ~160 fs pulses with the central wavelength of 800nm are used for photoexcitation/gating of the THz detectors and a ZnTe crystal is used for generation of THz pulses. In the other system, ~70 fs optical pulses with the central wavelength of 800nm are used for excitation/gating of the THz detector, and an InAs epilayer is used for generation of THz pulses. In both systems, the polarization of the optical excitation pulses incident on the THz detector is controlled by a λ/2 waveplate and a broadband polarizer (extinction ratio: 500:1). The THz beam is intensity modulated at 2.7 kHz using an optical chopper. The photocurrent from the THz detector is measured by a low-noise current amplifier (DL Instruments) and a lock-in amplifier (SR830). Details of the THz-TDS methodology can be found in[45].

ASSOCIATED CONTENT

*S Supporting Information

The Supporting Information (PDF) is available free of charge on the ACS Publications website at DOI: 10.1021/acs.nanolett.8b05118.

Supporting Figures S1−2 illustrate fabricated metasurfaces and THz detectors; and an estimation of the effect of resonance excitation with Supporting Figure 3 provide an explanation for polarization dependence of the frequency response of the THz detector. Figures S4-6 provide evidence for coupling between the M_x and M_z magnetic dipoles, and Figure S7 provides a measurement of the Q-factor of the M_x and M_z magnetic dipole modes. Figure S8 compares the performance of the metasurface detector to the detector design in Mitrofanov *et al*.[28]

AUTHOR INFORMATION

Corresponding Author

*o.mitrofanov@ucl.ac.uk

Author Contributions

O.M and I.B. conceived the idea. T.S. P.V. and L.H. simulated the metasurface properties and optimized the metasurface design. J.L.R grew LT GaAs, and O.M. fabricated the metasurface samples and the THz detectors. T.S., T.S.L, C.T.H, and O.M. set up experimental systems and performed device characterization. T.S. and O.M analyzed the experimental data and prepared illustrations. All authors contributed to the discussion of the results and to the editing of the manuscript. O.M. coordinated the overall research.

ACKNOWLEDGMENT

This work was supported by the EPSRC (EP/L015277/1, EP/P021859/1, EP/L015455/1) and by the U.S. Department of Energy, Office of Basic Energy Sciences, Division of Materials Sciences and Engineering. Fabrication, optical and, in part, THz experiments were performed at the Center for Integrated Nanotechnologies, an Office of Science User Facility operated for the U.S. Department of Energy (DOE) Office of Science. Sandia National Laboratories is a multi-mission laboratory managed and operated by National Technology and Engineering Solutions of Sandia, LLC., a wholly owned subsidiary of Honeywell International, Inc., for the U.S. Department of Energy's National Nuclear Security Administration under contract DE-NA-0003525. This article describes objective technical results and analysis. The views expressed in the article do not necessarily represent the views of the U.S. DOE or the United States Government.

REFERENCES

(1) Nagatsuma, T.; Ducournau, G.; Renaud, C. C. Advances in Terahertz Communications Accelerated by Photonics. *Nat. Photonics* **2016**, *10* (6), 371–379.

(2) Koenig, S.; Lopez-Diaz, D.; Antes, J.; Boes, F.; Henneberger, R.; Leuther, A.; Tessmann, A.; Schmogrow, R.; Hillerkuss, D.; Palmer, R.; et al. Wireless Sub-THz Communication System with High Data Rate. *Nat. Photonics* **2013**, *7* (12), 977–981.

(3) Tonouchi, M. Cutting-Edge Terahertz Technology. *Nat. Photonics* **2007**, *1* (2), 97–105.

(4) Karl, N. J.; McKinney, R. W.; Monnai, Y.; Mendis, R.; Mittleman, D. M. Frequency-Division Multiplexing in the Terahertz Range Using a Leaky-Wave Antenna. *Nat. Photonics* **2015**, *9* (11), 717–720.

(5) Meijer, A. S.; Berden, G.; Arslanov, D. D.; Ozerov, M.; Jongma, R. T.; van der Zande, W. J. An Ultrawide-Bandwidth Single-Sideband Modulator for Terahertz Frequencies. *Nat. Photonics* **2016**, *10* (11), 740–744.

(6) Chen, H.-T.; Padilla, W. J.; Cich, M. J.; Azad, A. K.; Averitt, R. D.; Taylor, A. J. A Metamaterial Solid-State Terahertz Phase Modulator. *Nat. Photonics* **2009**, *3* (3), 148–151.

(7) Carpinero, G. Semiconductor Terahertz Technology : Devices and Systems at Room Temperature Operation. Wiley-IEEE Press 2015.

(8) Castro-Camus, E.; Alfaro, M. Photoconductive Devices for Terahertz Pulsed Spectroscopy:

A Review. *Photonics Res*. **2016**, *4* (3), A36.

(9) Yardimci, N. T.; Jarrahi, M. Nanostructure-Enhanced Photoconductive Terahertz Emission and Detection. *Small* **2018**, *14* (44), 1802437.

(10) Lepeshov, S.; Gorodetsky, A.; Krasnok, A.; Toropov, N.; Vartanyan, T. A.; Belov, P.; Alú, A.; Rafailov, E. U. Boosting Terahertz Photoconductive Antenna Performance with Optimised Plasmonic Nanostructures. *Sci. Rep*. **2018**, *8* (1), 6624.

(11) Heshmat, B.; Pahlevaninezhad, H.; Pang, Y.; Masnadi-Shirazi, M.; Burton Lewis, R.; Tiedje, T.; Gordon, R.; Darcie, T. E. Nanoplasmonic Terahertz Photoconductive Switch on GaAs. *Nano Lett*. **2012**, *12* (12), 6255–6259.

(12) Berry, C. W.; Wang, N.; Hashemi, M. R.; Unlu, M.; Jarrahi, M. Significant Performance Enhancement in Photoconductive Terahertz Optoelectronics by Incorporating Plasmonic Contact Electrodes. *Nat. Commun*. **2013**, *4* (1), 1622.

(13) Jafarlou, S.; Neshat, M.; Safavi-Naeini, S. A Hybrid Analysis Method for Plasmonic Enhanced Terahertz Photomixer Sources. *Opt. Express* **2013**, *21* (9), 11115.

(14) Jooshesh, A.; Smith, L.; Masnadi-Shirazi, M.; Bahrami-Yekta, V.; Tiedje, T.; Darcie, T. E.; Gordon, R. Nanoplasmonics Enhanced Terahertz Sources. *Opt. Express* **2014**, *22* (23), 27992.

(15) Mitrofanov, O.; Brener, I.; Luk, T. S.; Reno, J. L. Photoconductive Terahertz Near-Field Detector with a Hybrid Nanoantenna Array Cavity. *ACS Photonics* **2015**, *2* (12), 1763–1768.

(16) Jooshesh, A.; Bahrami-Yekta, V.; Zhang, J.; Tiedje, T.; Darcie, T. E.; Gordon, R. Plasmon-Enhanced below Bandgap Photoconductive Terahertz Generation and Detection. *Nano Lett*. **2015**, *15* (12), 8306–8310.

(17) Billet, M.; Latzel, P.; Pavanello, F.; Ducournau, G.; Lampin, J.-F.; Peytavit, E. Resonant Cavities for Efficient LT-GaAs Photoconductors Operating at $\lambda = 1550$ Nm. *APL Photonics* **2016**, *1* (7), 076102.

(18) Yardimci, N. T.; Jarrahi, M. High Sensitivity Terahertz Detection through Large-Area Plasmonic Nano-Antenna Arrays. *Sci. Rep*. **2017**, *7*, 42667.

(19) Mohandas, R. A.; Freeman, J. R.; Natrella, M.; Rosamond, M. C.; Ponnampalam, L.; Fice, M. J.; Seeds, A. J.; Cannard, P. J.; Robertson, M. J.; Moodie, D. G.; et al. Terahertz Generation Mechanism in Nano-Grating Electrode Photomixers on Fe-Doped InGaAsP. *Opt. Express* **2017**, *25* (9), 10177.

(20) Thompson, R. J.; Siday, T.; Glass, S.; Luk, T. S.; Reno, J. L.; Brener, I.; Mitrofanov, O. Optically Thin Hybrid Cavity for Terahertz Photo-Conductive Detectors. *Appl. Phys. Lett*. **2017**, *110* (4), 041105.

(21) Kuznetsov, A. I.; Miroshnichenko, A. E.; Brongersma, M. L.; Kivshar, Y. S.; Luk'yanchuk, B. Optically Resonant Dielectric Nanostructures. *Science* **2016**, *354* (6314), aag2472.

(22) Genevet, P.; Capasso, F.; Aieta, F.; Khorasaninejad, M.; Devlin, R. Recent Advances in Planar Optics: From Plasmonic to Dielectric Metasurfaces. *Optica* **2017**, *4* (1), 139.

(23) Wu, C.; Arju, N.; Kelp, G.; Fan, J. A.; Dominguez, J.; Gonzales, E.; Tutuc, E.; Brener, I.; Shvets, G. Spectrally Selective Chiral Silicon Metasurfaces Based on Infrared Fano Resonances. *Nat. Commun.* **2014**, *5* (1), 3892.

(24) Campione, S.; Liu, S.; Basilio, L. I.; Warne, L. K.; Langston, W. L.; Luk, T. S.; Wendt, J. R.; Reno, J. L.; Keeler, G. A.; Brener, I.; et al. Broken Symmetry Dielectric Resonators for High Quality Factor Fano Metasurfaces. *ACS Photonics* **2016**, *3* (12), 2362–2367.

(25) Vabishchevich, P. P.; Liu, S.; Sinclair, M. B.; Keeler, G. A.; Peake, G. M.; Brener, I. Enhanced Second-Harmonic Generation Using Broken Symmetry III–V Semiconductor Fano Metasurfaces. *ACS Photonics* **2018**, *5* (5), 1685–1690.

(26) Liu, S.; Vaskin, A.; Addamane, S.; Leung, B.; Tsai, M.-C.; Yang, Y.; Vabishchevich, P. P.; Keeler, G. A.; Wang, G.; He, X.; et al. Light-Emitting Metasurfaces: Simultaneous Control of Spontaneous Emission and Far-Field Radiation. *Nano Lett.* **2018**, *18* (11), 6906–6914.

(27) Xu, X.; Kwon, H.; Gawlik, B.; Mohammadi Estakhri, N.; Alù, A.; Sreenivasan, S. V.; Dodabalapur, A. Enhanced Photoresponse in Metasurface-Integrated Organic Photodetectors. *Nano Lett.* **2018**, *18* (6), 3362–3367.

(28) Mitrofanov, O.; Siday, T.; Thompson, R. J.; Luk, T. S.; Brener, I.; Reno, J. L. Efficient Photoconductive Terahertz Detector with All-Dielectric Optical Metasurface. *APL Photonics* **2018**, *3* (3), 51703–51703.

(29) Chong, Y. D.; Ge, L.; Cao, H.; Stone, A. D. Coherent Perfect Absorbers: Time-Reversed Lasers. *Phys. Rev. Lett.* **2010**, *105* (5), 053901.

(30) Baranov, D. G.; Krasnok, A.; Shegai, T.; Alù, A.; Chong, Y. Coherent Perfect Absorbers: Linear Control of Light with Light. *Nat. Rev. Mater.* **2017**, *2* (12), 17064.

(31) Alaee, R.; Albooyeh, M.; Rockstuhl, C. Theory of Metasurface Based Perfect Absorbers. *J. Phys. D. Appl. Phys.* **2017**, *50* (50), 503002.

(32) Wan, W.; Chong, Y.; Ge, L.; Noh, H.; Stone, A. D.; Cao, H. Time-Reversed Lasing and Interferometric Control of Absorption. *Science* **2011**, *331* (6019), 889–892.

(33) Zhou, H.; Zhen, B.; Hsu, C. W.; Miller, O. D.; Johnson, S. G.; Joannopoulos, J. D.; Soljačić, M. Perfect Single-Sided Radiation and Absorption without Mirrors. *Optica* **2016**, *3* (10), 1079.

(34) Kats, M. A.; Capasso, F. Optical Absorbers Based on Strong Interference in Ultra-Thin Films. *Laser Photonics Rev.* **2016**, *10* (5), 735–749.

(35) Cole, M. A.; Powell, D. A.; Shadrivov, I. V. Strong Terahertz Absorption in All-Dielectric Huygens' Metasurfaces. *Nanotechnology* **2016**, *27* (42), 424003.

(36) Ming, X.; Liu, X.; Sun, L.; Padilla, W. J. Degenerate Critical Coupling in All-Dielectric

Metasurface Absorbers. *Opt. Express* **2017**, *25* (20), 24658.

(37) Piper, J. R.; Liu, V.; Fan, S. Total Absorption by Degenerate Critical Coupling. *Appl. Phys. Lett.* **2014**, *104* (25), 251110.

(38) Kuznetsov, A. I.; Miroshnichenko, A. E.; Fu, Y. H.; Zhang, J.; Luk'yanchuk, B. Magnetic Light. *Sci. Rep.* **2012**, *2* (1), 492.

(39) Lumerical Inc. Http://Www.Lumerical.Com/Tcad-Products/Fdtd/.

(40) Limonov, M. F.; Rybin, M. V.; Poddubny, A. N.; Kivshar, Y. S. Fano Resonances in Photonics. *Nat. Photonics* **2017**, *11* (9), 543–554.

(41) Koshelev, K.; Lepeshov, S.; Liu, M.; Bogdanov, A.; Kivshar, Y. Asymmetric Metasurfaces with High- Q Resonances Governed by Bound States in the Continuum. *Phys. Rev. Lett.* **2018**, *121* (19), 193903.

(42) Hsu, C. W.; Zhen, B.; Stone, A. D.; Joannopoulos, J. D.; Soljačić, M. Bound States in the Continuum. *Nat. Rev. Mater.* **2016**, *1* (9), 16048.

(43) Volatier, M.; Duchesne, D.; Morandotti, R.; Arès, R.; Aimez, V. Extremely High Aspect Ratio GaAs and GaAs/AlGaAs Nanowaveguides Fabricated Using Chlorine ICP Etching with N_2 -Promoted Passivation. *Nanotechnology* **2010**, *21* (13), 134014.

(44) Mitrofanov, O.; Brener, I.; Wanke, M. C.; Ruel, R. R.; Wynn, J. D.; Bruce, A. J.; Federici, J. Near-Field Microscope Probe for Far Infrared Time Domain Measurements. *Appl. Phys. Lett.* **2000**, *77* (4), 591.

(45) Mitrofanov, O.; Lee, M.; Hsu, J. W. P.; Brener, I.; Harel, R.; Federici, J. F.; Wynn, J. D.; Pfeiffer, L. N.; West, K. W. Collection-Mode near-Field Imaging with 0.5-THz Pulses. *IEEE J. Sel. Top. Quantum Electron.* **2001**, *7* (4), 600–607.